Assessment of aerodynamic roughness parameters of turbulent boundary layers over barnacle-covered surfaces

Takfarinas Medjnoun[1*], Manuel Ferreira[1], Ralf Reinartz[1], Bagus Nugroho[2], Jason Monty[2], Nicholas Hutchins[2] and Bharathram Ganapathisubramani[1]

[1*]Department of Aeronautics & Astronautics, University of Southampton, Burgess Road, Southampton, SO17 1BJ, Hampshire, United Kingdom.
[2]Department of Mechanical Engineering, University of Melbourne, Grattan Street, Parkville, 3010, Victoria, Australia.

*Corresponding author(s). E-mail(s): t.medjnoun@soton.ac.uk;
Contributing authors: m.aguiar-ferreira@soton.ac.uk; r.r.l.reinartz@tue.nl;
bagus.nugroho@unimelb.edu.au; montyjp@unimelb.edu.au; nhu@@unimelb.edu.au;
g.bharath@soton.ac.uk;

Abstract

Full-scale drag penalty predictions of flows over rough walls require surface roughness characterisation from laboratory experiments or numerical simulations. In either approach, it is necessary to determine the so-called equivalent sand-grain roughness height ($\boldsymbol{k_s}$). There are several steps involved in determining this aerodynamic roughness lengthscale, but its procedure typically includes a combination of measurement of wall-shear stress ($\boldsymbol{\tau_w}$) using direct or indirect methods as well as analysis of velocity profiles. Indirect methods usually rely on assumptions made about flow and its scaling including the validity of universal outer-layer similarity. However, the implications of the underlying assumptions involved in full-scale drag prediction are unclear. In this work, we carry out wind tunnel measurements over a realistic rough surface (from a fouled ship-hull) to evaluate the impact of different methods with an emphasis on using the outer-layer similarity hypothesis for full-scale drag predictions. Wall-shear stress is measured using an in-house floating-element drag balance (DB) and velocity profiles are obtained using particle image velocimetry (PIV), allowing the evaluation of $\boldsymbol{k_s}$, and the associated wake parameters through several methods. The aerodynamic roughness parameters hence obtained, are used for full-scale drag penalty calculations. It is observed that the predicted drag penalty can vary by over 15% among the different methods highlighting the care that should be taken when employing such methods.

Keywords: turbulent boundary layers, roughness, drag

1 Introduction

The skin friction drag is well-established as one the most valuable quantities characterising smooth- and rough-wall bounded flows, as it embodies the result of the conversion of the free stream momentum into shear force by means of the boundary layer. Considering the ever-increasing interest in reducing the carbon footprint and the

environmental impact of fuel-based systems, accurate measurement and prediction of this quantity remain vital to a whole range of engineering applications (e.g. design of aerodynamically efficient vehicles). Skin friction is equally important for researchers as it influences strongly the fluid motion near the wall but is also crucial in understanding wall-turbulence dynamics due to its scaling capabilities for both the near- and outer-wall regions (Chung et al, 2021).

Regardless of whether the frictional drag is directly or indirectly measured, the use of similarity laws is required to scale up the information from laboratory measurements and/or numerical simulations to full-scale predictions. In this study, we specifically examine the use of four methods for the assessment of the aerodynamic roughness parameters with two methods using direct drag measurements and two indirect methods relying on flow assumptions, namely; Townsend's outer-layer similarity (OLS) hypothesis and the comprehensive shear stress (CSS) methods (Townsend, 1976; Womack et al, 2019). The results are subsequently scaled up from laboratory to full-scale to assess the impact on high Reynolds numbers using an integral boundary layer evolution method (Monty et al, 2016).

1.1 Background

Above the roughness sublayer, the mean flow over a rough wall is sufficiently captured through the log-wake law, similar to a smooth wall. Therefore, the mean velocity profile in inner and outer forms can be respectively written as,

$$\frac{U}{U_\tau} = \frac{1}{\kappa}\ln\left(\frac{(y-d)U_\tau}{\nu}\right) + B - \frac{\Delta U}{U_\tau} + \frac{\Pi}{\kappa}W\left(\frac{y}{\delta}\right), \quad (1)$$

$$\frac{U_\infty}{U_\tau} - \frac{U}{U_\tau} = -\frac{1}{\kappa}\ln\left(\frac{y-d}{\delta}\right) + \frac{\Pi}{\kappa}\left[2 - W\left(\frac{y}{\delta}\right)\right], \quad (2)$$

where y is the wall-normal location whose origin is taken as the lowest roughness height (h_{min}), U_∞ is the freestream velocity, U is the mean streamwise velocity, $U_\tau = \sqrt{\tau_w/\rho}$ is the skin-friction velocity (τ_w is the wall-shear-stress and ρ is the density of the fluid) and the boundary layer thickness δ is defined as the wall-normal height where $U \approx 0.99U_\infty$, ν is the fluid kinematic viscosity. In the above equations, the inner-normalised velocity deficit in the log region $\Delta U/U_\tau \equiv \Delta U^+$ is known as the roughness function (Hama, 1954) and depends on the nature of the surface roughness. d is a virtual origin (also referred to as the zero-plane displacement) representing the height at which the mean momentum sink occurs (Jackson, 1981), and similarly depends on the roughness. Both ΔU^+ and d are equal to zero for a smooth wall. The logarithmic region is described by its slope κ, paired with its smooth-wall intercept B. However, it has been shown that these "constants" vary depending on the flow geometry with κ ranging from 0.37 to 0.41 between turbulent channel, boundary layer, and pipe flows (Nagib and Chauhan, 2008).

Beyond the log layer, an overshoot of the velocity from the logarithmic behaviour occurs and is believed to emanate from a dual effect of the velocity jumps in the uniform momentum zones as well as the jump across the turbulent/non-turbulent interface (Krug et al, 2017). This is described by the term $W(y/\delta)$ known as the Coles wake function (Coles, 1956), which is characterised by its wake strength parameter Π. There have been numerous studies in the literature that proposed analytical expressions to capture this region, and depending on the expression, the same flow yields different estimates of Π (see for example Jones et al (2001); Guo et al (2005); Nagib et al (2007) for reference). In fact, for a given κ and B, Π in a zero-pressure gradient turbulent boundary layer is reported to be around 0.55, 0.65, and 0.45 for the expressions used by Hinze (1975), Jones et al (2001) and Nagib et al (2007), respectively. Therefore, comparing the wake strength parameter is only meaningful when the same expression is used. Moreover, for a given wake function, Π is also sensitive to pressure gradients, with Π increasing and decreasing with adverse and favourable pressure gradients, respectively.

By adding equation 1 and 2, an expression for the skin-friction coefficient can be obtained, and is given by,

$$U_\infty^+ = \sqrt{\frac{2}{C_f}} = \frac{1}{\kappa}\ln(\delta^+) + B - \Delta U^+ + 2\frac{\Pi}{\kappa}, \quad (3)$$

with the superscript "+" denoting quantities non-dimensionalised by U_τ and ν. Assuming κ and B universal constants, expression 3 clearly shows that $C_f = f(\delta^+, \Delta U^+, \Pi)$, with $\delta^+ \equiv Re_\tau = U_\tau \delta/\nu$ being the friction Reynolds number. Therefore, the accuracy in determining the constitutive quantities of C_f can have serious implications on the prediction of skin friction and drag penalty at high Reynolds numbers. In this study, ΔU^+ and Π will be evaluated through different methods, allowing us to quantitatively assess their resulting predictions.

1.2 Outer-layer similarity

Over rough walls, outer-layer similarity (OLS) emerges as an extension of Townsend's wall-similarity hypothesis, which states that the influence of viscosity is limited to the near-wall region (Townsend, 1976). In this scenario, roughness effects are hypothesised to be confined to the near-wall region, provided the roughness length scale (k - representative roughness height) is a small portion of δ (i.e. k/δ is small). In other words, a large separation between scales is required ($1 \ll k^+ \ll \delta^+$). This means that in the wake region, the mean and the turbulence motions can be assumed to have a universal form between smooth- and rough walls. This is generally expressed in a functional form as

$$\frac{U_\infty - U}{U_\tau} = f\left(\frac{y}{\delta}\right), \qquad \frac{\overline{u_i u_j}}{U_\tau^2} = g_{ij}\left(\frac{y}{\delta}\right). \quad (4a, b)$$

This means that the role of roughness is limited to the adjustment of the friction velocity (U_τ) and the boundary layer thickness (δ), while the mean and turbulence structure functions (f) and (g_{ij}), respectively, remain unaffected. From the early work of Perry and Abell (1977) on roughened pipe flows, numerous studies have shown the presence of outer-layer similarity in rough-wall flows over various surface conditions (Andreopoulos and Bradshaw, 1981; Acharya et al, 1986; Perry and Li, 1990; Raupach, 1992; Schultz and Flack, 2005; Castro, 2007; Wu and Christensen, 2007; Squire et al, 2016). However, other researchers have also reported cases where rough-walls do not behave similarly to smooth-wall flows under certain circumstances (Krogstad et al, 1992; Krogstad and Antonia, 1994; Volino et al, 2009; Chan et al, 2018; Chung et al, 2018; Medjnoun et al, 2018, 2020; Womack et al, 2022).

Intuitively, the relative height of the roughness (k/δ with k being a representative roughness height) is suggested to be particularly important for a flow to follow outer-layer similarity, with several works proposing thresholds with a minimum of $\delta/k > 10$ (Jimenez, 2004; Schultz and Flack, 2005). However, the results outlined by Flack et al (2007) and later by Amir and Castro (2011) clearly indicated that outer-layer similarity can still be valid even at $\delta/k < 10$ suggesting that a single critical roughness height beyond which outer-layer similarity fails does not necessarily exist. They argued that the outer flow is only gradually altered with increasing roughness height. Nonetheless, there is growing evidence from both recent experimental and numerical studies that suggest similarity remains strongly dependent not only on roughness amplitude but also on other parameters such as its phase and directionality (Chung et al, 2021), suggesting that universal similarity might not be possible for some types of surface roughness. Therefore, it is important to examine the implications of this hypothesis when drag penalty predictions are desired and provide corrections if necessary.

1.3 Roughness function

The skin-friction law in equation 3 can be written for a rough- and a smooth-wall ($\Delta U^+ = 0$) and subtracted from each other to determine the roughness function expression:

$$\Delta U^+ = \overbrace{\sqrt{\frac{2}{C_f^S}} - \sqrt{\frac{2}{C_f^R}}}^{\mathrm{I}} + \overbrace{\frac{1}{\kappa}\ln\left(\frac{\delta^{+R}}{\delta^{+S}}\right)}^{\mathrm{II}} + \overbrace{2\frac{(\Pi^R - \Pi^S)}{\kappa}}^{\mathrm{III}}, \quad (5)$$

with the superscripts S and R identifying quantities measured over smooth and rough wall flow conditions, respectively. Under the current hypotheses, equation 5 shows that the roughness function is characterised by three main contributions. The term I) represents the roughness function contribution stemming from the change in frictional drag between surfaces, the term II) captures the contribution arising due to the difference in the frictional Reynolds numbers, whereas the term III) shows the roughness function contribution caused by the alteration in the wake strength parameter. In equation 5, the function governing the wake W in the outer flow is assumed to be universal (i.e. universal form), however, the wake strength (i.e. the amplitude of the function) can be different between surfaces, and it is captured by its wake strength parameter. In fact, changes in the outer flow are usually reflected in different values of Π for different surface conditions. Therefore, an accurate assessment of the roughness function requires accurate knowledge of the different constitutive terms that characterise the roughness function.

If $\Pi^R = \Pi^S$, then there is universal outer-layer similarity. In this instance, ΔU^+ can still be determined by substituting the two different values of δ^+ in equation 5. This is identical to the procedure used by Granville (1987), and with some further manipulations, the integrated skin-friction coefficient C_F over a plate of length L can be obtained. If also ${\delta^+}^R$ and ${\delta^+}^S$ are matched in the presence of universal outer-layer similarity, then ΔU^+ reduces to the difference in the frictional drag, and can be obtained from direct wall-shear stress measurements, and is expressed as:

$$\Delta U^+ \equiv \Delta U^+_{DB} = \sqrt{\frac{2}{C_f^S}} - \sqrt{\frac{2}{C_f^R}} \qquad (6)$$

with the subscript, DB representing the quantity measured directly using the drag balance technique, used in this study. The skin friction coefficient C_f^S for the smooth wall can be separately measured or obtained from the smooth-wall expression (i.e. equation 3).

In the absence of direct skin-friction measurements, velocity profile data are required. It is a common practice for studies on rough-wall flows to infer the aerodynamic quantities from a fitting procedure of the logarithmic velocity data, or the total shear stress profile (Perry and Li, 1990; Krogstad et al, 1992; Flack et al, 2005; Schultz and Flack, 2005; Flack et al, 2007; Wu and Christensen, 2007). Alternatively, the use of Townsend's similarity hypothesis enables estimating U_τ from the outer flow, however, with the assumption that similarity does exist. It is only in some isolated facilities such as in towing tanks and a few wind tunnels where direct drag information has been used to determine ΔU^+ (Cheng and Castro, 2002; Schultz and Myers, 2003; Krogstad and Efros, 2010; Baars et al, 2016; Ferreira et al, 2018). Their limited use is essentially due to their manufacturing cost as well as the delicate attention needed when operating such devices.

However, while it is possible to use equation 6 to determine ΔU^+ under certain conditions (matched δ^+ and presence of OLS), in practice, both conditions cannot be *a-priori* assumed without examining the flow. Hence, in the absence of a guarantee that outer-layer similarity can be valid for a given rough surface, velocity profile measurements are essential to measuring all relevant quantities and ensuring appropriate predictions are possible. When velocity information is available, the roughness function can be determined from the shift in the log region, relative to the smooth-wall profile, directly from the inner-scaled velocity distribution. In fact, the value of ΔU^+ hence determined represents the momentum loss or gain (in case of drag reduction) and is the correct estimate of the roughness function, provided there is an independent (direct) estimate of U_τ.

Once ΔU^+ is determined from drag, velocity measurements, or both, the rough surface is exposed to different freestream speeds to obtain the variation of ΔU^+ as a function of the aerodynamic roughness lengthscale. By evaluating ΔU^+ as a function of k_s^+, the equivalent sand-grain roughness height k_s can be determined using the expression:

$$\Delta U^+ \text{ or } \Delta U^+_{DB} = \frac{1}{\kappa}\ln(k_s^+) - C \qquad (7)$$

where, C is an additive constant, determined empirically to be equal to 3.5 (Nikuradse, 1933). Combining equation 7 together with 3, an expression for fully-rough flows can be written as:

$$k_s = \delta \exp\left(2\Pi^{\mathrm{R}} - \kappa\left[\sqrt{\frac{2}{\mathrm{C_f^R}}} - \mathrm{B_R}\right]\right). \quad (8)$$

Equation 8 shows that k_s depends on the boundary layer thickness δ (with δ being also a function of x for boundary-layers), the rough wake strength parameter Π^R (with $\Pi^R = \Pi^S$ if OLS is satisfied), the rough-wall intercept B_R (with $B_R = B + C$) and the skin-friction coefficient C_f. The quantity k_s does not represent a geometrical lengthscale of the roughness but rather an aerodynamic property of the rough-wall flow investigated. Hence, it can only be determined with the assessment of the flow, and as such, equation 7 or 8 require the flow to be exposed to a range of Reynolds numbers to detect whether the data has reached an asymptotic behaviour. If the roughness function follows the trend in either equation 7 or 8, then the flow over the surface is considered to be "fully rough", and k_s can subsequently be used to predict the drag penalty at higher Reynolds numbers. For the purposes of this study, we assume the flow to be "fully rough" if the skin-friction coefficient C_f is invariant with Reynolds number (i.e. data can fit equation 7). It is also worth recalling that boundary layer flows are always developing, and their C_f and δ (perhaps even Π) remain a function of the streamwise distance x. Therefore, the assessment of k_s in this study is associated with a fixed streamwise location.

1.4 Contribution and outline

It is evident that in the absence of direct drag measurements, determination of the skin friction hence $\Delta U^+(k_s)$ can only be achieved using velocity profile data at the price of either assuming the validity of outer-layer similarity or other alternative ways such as the modified Clauser-chart (which requires fittings U_τ, d and ΔU^+ while fixing κ and B in equation 1) or total shear stress methods. The choice of either will most certainly affect the drag prediction at higher Reynolds numbers. However, the implications of these steps and assumptions on the final prediction remain unclear.

In this work, direct drag measurements are carried out using an in-house floating element drag balance previously validated by Ferreira et al (2018), while velocity field measurements are performed using particle image velocimetry. The experiments are performed over a realistic rough surface with the objective of examining the limitations of indirect methods in determining the equivalent sand-grain roughness height. Once the value of k_s is determined, it is possible to make predictions of the total frictional drag (C_F) at higher Reynolds numbers using the integral boundary layer evolution equations as outlined by Monty et al (2016), which in turn will allow the estimation of the total ship resistance. We also compare the results from indirect methods in determining the aerodynamic roughness parameters and examine the implications of using them for drag penalty predictions at high Reynolds numbers over moderately fouled ship hull surfaces. The different methods used in this study are summarised in table 1.

The remainder of the manuscript is presented in three sections. The experimental methodology is described in section 2 depicting the roughness topography, drag, and flow field measurement techniques. The results and discussion are reported in section 3, presenting direct drag measurements and the various methods used to evaluate k_s. It is followed by a discussion on the influence of different methods on drag penalty predictions at high Reynolds numbers. A summary and some concluding remarks are provided in section 4. An appendix is also provided at the end of the manuscript, reporting a detailed uncertainty analysis of the aerodynamic roughness parameters. The results presented in this study will be made openly accessible on the roughness database http://roughnessdatabase.org/ and the University of Southampton repository, upon publication.

2 Experimental Methods

2.1 Facility and biofouling roughness

Measurements are conducted in an open-circuit suction-type wind tunnel at the University of Southampton. The test section is 0.6 m $\times$ 0.9 m in the (y, z) cross-plane and spans 4.5 m in the x-wise direction, following a 7:1 contraction. The test section was designed with a weak diverging cross-section to allow a constant free stream along the streamwise direction and the growth

Table 1 Methods used for the current case study of biofouled rough-wall flow.

Method	wall-shear stress	flow
Method 1: DB	drag balance	assumed (equation 6)
Method 2: Direct	drag balance	PIV
Method 3: OLS	outer-layer similarity (Townsend, 1976)	PIV
Method 4: CSS	comprehensive shear stress (Womack et al, 2019)	PIV

of a turbulent boundary layer with a nominally zero pressure gradient. The acceleration parameter $K = \frac{\nu}{U_\infty}\frac{dU_\infty}{dx}$, was shown to range between $1{-}5{\times}10^{-8}$ from various recent studies performed in this facility (Ferreira and Ganapathisubramani, 2021; Medjnoun et al, 2021). The turbulent boundary layer develops over a flat surface composed of five equally-sized wooden boards onto which the biofouled surface roughness is mounted. In order to assess the skin friction, a 0.2 m × 0.2 m slot was made in one of the boundary layer plates at the measurement location to accommodate the floating element drag balance. The boundary layer plates are preceded by a ramp of 0.2 m long inclined by four degrees to the horizontal, ensuring a smooth transition of the flow from the bottom floor of the test section. The free stream speed can reach up to 30 ms^{-1}, with a turbulence level less than 0.5%, and is monitored and acquired using a micromanometer FC510. To account for air density variations, the temperature is also acquired, and its standard deviation for an average run was less than $\pm 0.5^o$ Celsius.

The roughness was made of a tiled surface manufactured from a moderately fouled coupon. The coupon is taken from a dry-dock silicone mould obtained directly from a ship hull. The coupon consists of some tubeworm fouling as well as one barnacle. The size of the coupon was 25 mm × 50 mm and this was repeated in two directions to generate a repeating-unit tile of 100 mm × 100 mm. The surface properties of the coupon are also listed in the left panel of table 2 while the surface topography is shown on the right panel. To manufacture these surfaces, four master tiles are initially 3D printed using a Formlab Resin printer with a height resolution of 10 μm equivalent to one viscous scale at the highest Reynolds number of the facility. These master tiles were used to create several silicone moulds, which were subsequently used to cast over 400 replicas of polyester resin needed to cover the entire floor of the wind tunnel test section. The boards are mounted in two configurations in the wind tunnel generating two different roughness patterns from the same tiles, which can be depicted by the directionality of effective slopes ES (Napoli et al, 2008) as shown in table 2. Therefore, the spanwise characteristic wavelength of Config 1 is equal to the streamwise wavelength of Config 2, and *vice-versa* ($S_{z,1} = S_{x,2} = 50$ mm and $S_{z,2} = S_{x,1} = 25$ mm).

2.2 Floating-element drag balance

Wall shear stress is directly measured using the floating-element drag balance developed and validated by Ferreira et al (2018). Its design is based on the parallel-shift linkage, featuring dedicated pairs of bending-beam transducers to monitor not only the streamwise load but also the induced pitching moment, as a means to decouple extraneous loads. The balance itself is a 200-mm-side square that is small enough in relative terms to ensure local measurements of wall shear stress. The balance is flush mounted with the wind tunnel floor, roughly 3.2 m downstream of the contraction. Special care was taken to mounting the surrounding tiles of the balance, given the tight tolerance of the fix-to-floating surface joint that is only 0.5 mm wide. It is emphasised that the dimensions of the balance are a multiple of a tile size, which is 100-mm-side square. Therefore, on the floating element, four complete tiles were placed.

In order to determine C_f^R as a function of the Reynolds number and determine the aerodynamic roughness lengthscale of the rough surface, the floating element is subjected to a series of nine free stream velocities ranging from 9 up to 27 ms^{-1}. Each acquisition lasted 30 s sampled at 150 Hz, equivalent to 2500 boundary-layer eddy turnover times ($\tau_{eddy} = \delta/U_\infty$) at the lowest operating speed, with a total of five repetitions per velocity. Pre- and post-calibrations were conducted for

Table 2 (left) Key surface parameters from the scanned coupon, where h' represents the surface elevation of the topography about the mean height ($h'(x,z) = h(x,z) - \overline{h}$). (right) The surface topography of a single repeating unit was used for the experiments. Measurements are carried out in two different configurations as shown with Config 1 having a streamwise characteristic wavelength ($S_{x,1}$) between barnacles of 50 mm while Config 2 has a wavelength ($S_{x,2}$) of 25 mm. Note that $S_{x,1} = 2S_{z,1}$ and $S_{x,2} = S_{z,2}/2$. The influence of surface directionality is highlighted in the effective slope ES with $ES_{x,1}$ and $ES_{x,2}$ representing the streamwise effective slopes for Config 1 and Config 2, respectively. Hence, the streamwise effective slope of Config 1 is equal to the spanwise effective slope of Config 2 and *vice-versa*.

Parameters	Value	Units	Definition
k_m	1.03	mm	$\overline{h}$
k_{rms}	1.17	mm	$\sqrt{\overline{(h')^2}}$
k_p	6.25	mm	h_{max}-h_{min}
k_{sk}	2.57	-	$\overline{(h')^3}/k_{rms}^3$
k_{ku}	9.35	-	$\overline{(h')^4}/k_{rms}^4$
$S_{x,1}$	50	mm	x-wise wavelength
$S_{x,2}$	25	mm	x-wise wavelength
$ES_{x,1}$	0.46	-	$\mid \overline{dh'/dx} \mid$
$ES_{x,2}$	0.40	-	$\mid \overline{dh'/dx} \mid$

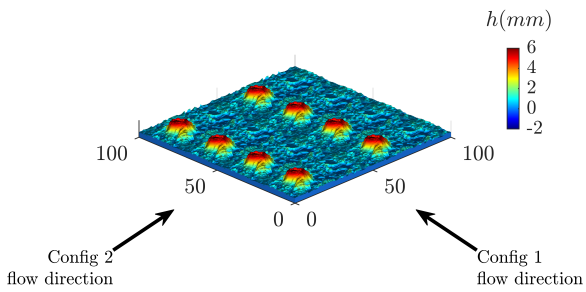

each configuration with a change in the calibration coefficient less than 0.5%. The acquisition procedure and uncertainty analysis are detailed in Ferreira et al (2018).

2.3 Particle image velocimetry

In order to examine the flow, velocity fields are obtained from both planar and stereoscopic particle image velocimetry (PIV) measurements at a similar location to that of the drag measurements. All planar and stereoscopic PIV measurements are performed in the (x,y)- and (y,z)-planes respectively. For the first surface configuration, seven PIV measurements are taken at various free stream speeds ranging from 7 up to 23 ms^{-1}. This included six planar-PIV cases with five above the valley (between two successive barnacle centres) and one additional plane at the centre of barnacles, while one stereo-PIV plane was also taken above the barnacles. For the second surface configuration, another seven PIV measurements are also acquired at similar free stream speeds to the first configuration. This consisted of five stereo-PIV planes at the top of the barnacles with two additional planar-PIV cases; one at the top of the barnacles and another between them. A summary of the different cases is provided in table 3.

To trace the flow, vaporised glycerol-water particles produced by a Magnum 1200 fog machine are used, then illuminated with a laser-light sheet sourced by a two-pulse Litron Nd:YAG laser operating at 200 mJ. A LaVision optical system for the beam focus/expansion of the light sheet is employed, which is comprised of convex and concave lenses in order to focus the beam and a cylindrical lens in order to expand the sheet with relatively constant thickness in the measurement plane (roughly 1 mm thickness). The particle images are recorded by high-resolution LaVision Imager LM 16 MP CCD cameras fitted with 200 and 300 mm AF Micro Nikkor lenses for the planar- and stereo-PIV planes, respectively. One camera was used for the planar-PIV setup and is positioned at roughly 1 m away from the object plane, whereas two other cameras needed for stereo-PIV planes are mounted on Scheimpflug adapters to account for the oblique view angle ($\pm 42^o$), and placed at approximately 1.3 m from the object plane at either side of the test section. A single and a double-sided dual-plane calibration target aligned with the laser light sheet were used to determine the mapping function for each setup, using a third-order polynomial fit. This resulted in a field of view of nearly $0.9\delta \times 1.5\delta$ in the (x,y)-plane and $1.3\delta \times \delta$ in the (y,z)-plane for the planar and stereoscopic PIV, respectively.

For both configurations, 500 to 3000 independent realisations of image pairs are acquired for

Table 3 Experimental parameters and flow conditions for both configurations. The PIV and sPIV data refer to the (x, y) and (z, y) measurement planes while the subscripts $_p$ and $_v$ indicate the peak (barnacle's top) and valley (between barnacles) locations respectively.

Case	Data	Samples	U_∞ (ms^{-1})	δ (mm)	$C_f \times 10^3$	k_p/δ (%)	k_p/k_s
Config 1	PIV$_v$	500	7.76	108.1	7.83	5.78	0.54
	PIV$_v$	500	10.29	109.2	7.86	5.72	0.54
	PIV$_v$	500	12.75	110.4	7.87	5.66	0.54
	PIV$_v$	500	18.05	114.3	7.87	5.47	0.54
	PIV$_v$	3000	23.07	114.1	7.93	5.48	0.54
	PIV$_p$	3000	23.82	115.1	7.96	5.43	0.54
	sPIV$_p$	3000	18.25	113.8	7.87	5.49	0.54
Config 2	sPIV$_p$	500	7.61	105.0	7.13	5.96	0.77
	sPIV$_p$	500	10.35	106.2	7.12	5.89	0.77
	sPIV$_p$	500	13.70	106.2	7.10	5.89	0.77
	sPIV$_p$	3000	18.09	109.5	7.10	5.71	0.77
	sPIV$_p$	500	23.08	111.5	7.05	5.61	0.77
	PIV$_p$	1500	18.07	109.6	7.10	5.71	0.77
	PIV$_v$	1500	18.15	110.0	7.10	5.68	0.77

the Reynolds number sweep at 0.6 Hz, with a time delay ranging between 25 and 70 μs resulting in an average particle displacement of 20 pixels/s. The velocity vector fields are then obtained by interrogating particle images using a decreasing multipass scheme starting from 48 pixels $\times$ 48 pixels down to a final pass of 16 pixels $\times$ 16 pixels for the planar PIV and 24 pixels $\times$ 24 pixels for the stereo PIV. Using a 50% interrogation window overlap, the resulting effective vector spacing ranged between 0.2$-$0.4 mm, equivalent to an inner-normalised volume resolution of $\Delta x^+ \times \Delta y^+ \times \Delta z^+ \approx 7.4 \times 7.4 \times 32$ for the lowest Reynolds number up to $35.7 \times 35.7 \times 87.4$ for the highest Reynolds number (also depending on the different planar and stereoscopic PIV measurements).

3 Results

This section focuses on results reported from the analysis of the aerodynamic roughness parameters evaluated using different methods. Section 3.1 discusses the results obtained from the floating element and predicts the roughness lengthscale obtained from direct drag measurements together with equation 6. The second section 3.2 discusses the aerodynamic properties obtained using both direct drag and velocity measurements. Section 3.3 examines the effect of using indirect methods in the assessment of the aerodynamic properties of the roughness. Finally, section 3.4 attempts to reconcile these results by showing how discrepancies from different methods affect skin friction predictions at higher Reynolds numbers.

3.1 Method 1: DB + Equation 6

Figure 1 shows the variation in skin-friction coefficient for the two different configurations, alongside smooth wall data obtained using oil-film interferometry (OFI) in the same facility. These measurements were obtained at various free stream velocities and therefore the abscissa in figure 1(a) represents the Reynolds number Re_x at a fixed streamwise fetch (3.2 m downstream the leading edge of the surface roughness), while figure 1(b) shows the same data where PIV measurements are performed and plotted against the friction Reynolds number Re_τ. It is clear that both configurations of rough walls yield a much higher skin-friction coefficient than a smooth wall with an increase of 320% and 280% at $Re_x \approx 5 \times 10^6$ for Config 1 and Config 2, respectively. Both figures show that C_f has reached an asymptotic limit for each case as it appears to not change as the Reynolds number increases. This suggests that both surfaces have reached a fully-rough regime

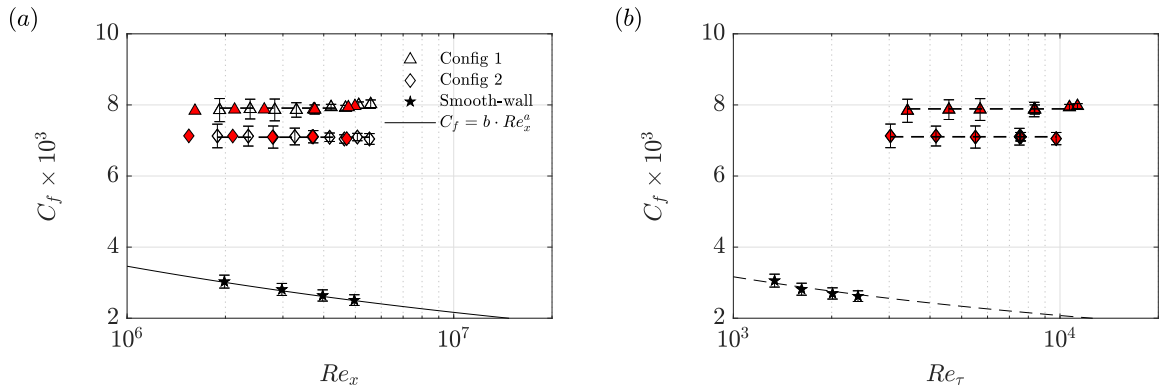

Fig. 1 (*a*) Variation of the skin-friction coefficient C_f measured using the drag balance with respect to Reynolds number Re_x for the two configurations, with the red-filled markers representing the interpolated values where the s/PIV measurements are performed . The black solid line indicates Schlichting's power law for smooth-wall with $a \approx -1/5$ and $b \approx 0.058$. The blue star symbols represent oil-film interferometry data from Medjnoun et al (2018). (*b*) The same data as in (*a*) is plotted against the friction Reynolds number Re_τ where PIV measurements are performed. The dashed line represents equation 3 applied for the smooth-wall ($\Delta U^+ = 0$) with $\Pi = 0.57$. The error bars include both systematic as well as random uncertainties in the measurements.

whereby the skin friction is invariant with the Reynolds number (for a given streamwise fetch).

Furthermore, the skin friction produced by surface Config 1 is 9.5% higher than that generated by Config 2. The difference can be attributed to the directional alignment present in the biofouled rough surface, as indicated by the effective slope (ES) in both streamwise and spanwise directions, despite both surfaces sharing similar statistical characteristics. Following the surveys of Napoli et al (2008) and Schultz and Flack (2009) on turbulent boundary layers over irregular and regular rough-walls, respectively, both current configurations can be considered to be within the roughness regime (roughness regime if $ES > 0.35$ and waviness regime otherwise). It is also seen that Config 1 has an effective slope 15% larger than that of Config 2. This result suggests that this drag increase could be due to contributions from an increase in the flow separation around steeper roughness features. It is also intuitive to assume that the drag can easily be influenced by the change in the spanwise/streamwise characteristic wavelengths S_x and S_z. However, the latter parameters have both changed from Config 1 to Config 2, and it would be impossible to ascertain which parameter had more impact in increasing the drag.

The skin-friction coefficient can be used to estimate the roughness function and hence the equivalent sand-grain roughness. Following equation 6 which assumes outer-layer similarity, the roughness function ΔU^+_{DB} can be determined from solely the friction velocity and boundary layer thickness information. The latter can easily be obtained with a quick survey of the mean flow using Pitot, hot-wire anemometry, or as in this study, PIV measurements. Since outer-layer similarity implies the wake strength parameters between smooth and rough walls to be matched ($\Pi^R = \Pi^S$), the roughness function ΔU^+_{DB} can be obtained by either matching δ^+ of both the smooth and rough-wall measurements or by simply adding the $\frac{1}{\kappa}\ln\left(\frac{\delta^{+R}}{\delta^{+S}}\right)$ term to equation 6 if the δ^+'s are unmatched. In fact, our results showed both methods yield identical ΔU^+_{DB} estimates.

Results of the roughness function ΔU^+_{DB} under the assumptions of equation 6 (matched δ^+ and Π between smooth and rough-wall flows) are depicted in figure 2(*a*) showing its variation with respect to k^+_{rms}. The outcome of choosing k_{rms} or any other representative roughness height remains the same in the determination of the equivalent sand grain roughness height $k_{s,DB}$. The results of the roughness function for both cases are shown to vary logarithmically with this length scale as a

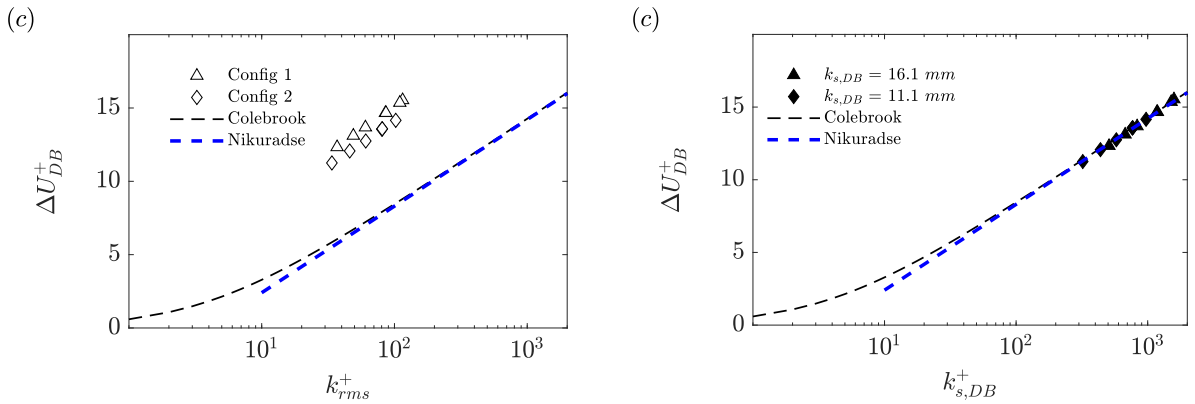

Fig. 2 (*a*) Variation of the roughness function ΔU^+_{DB} as a function k^+_{rms} with ΔU^+_{DB} determined from drag balance measurements and boundary layer thickness, using equation (1.5). (*b*) Variation of ΔU^+_{DB} with respect to $k^+_{s,DB}$ determined using equation 7 with the constant $C = 3.5$. The dashed black line is the correlation from Colebrook and White (1937) and the dashed blue line is the fully-rough asymptote from Nikuradse (1933). The values of $k_{s,DB}$ determined are indicated in the legend of the left figure.

consequence of the fully-rough regime observed in figure 1.

Using the appropriate value of $k_{s,DB}$, the same data can be collapsed to the fully-rough line represented by equation 7 as shown in figure 2(*b*). The results show that even at the lowest Reynolds number, all measurement points exhibit a $k^+_{s,DB} > 300$, well within the fully-rough regime. The large values in the reported $k^+_{s,DB}$ are a consequence of the corresponding large values in ΔU^+_{DB} (over 11 at the lowest Reynolds number) which can be considered as a strong roughness in both configurations. These surfaces are shown to lead to considerable values of $k_{s,DB}$ when compared with their geometrical attributes with $k_{s,DB} \approx 2.6k_p$ and $k_{s,DB} \approx 1.8k_p$ or approximately 15% and 10% when expressed as a fraction of the boundary layer thickness for Config 1 and Config 2, respectively. The subsequent analysis will investigate how the roughness function and other aerodynamic parameters obtained from velocity measurements compare with the values presented above.

3.2 Method 2: DB + PIV

Although PIV fields are not shown here for brevity, results for both configurations indicate that the mean and turbulent flow heterogeneity remain confined within the roughness sublayer ($y < 0.1\delta$) in both the (x, y)- and (y, z)-planes, demonstrating that these surfaces (flows) behave as homogeneous rough surfaces (flows). Hence, the subsequent results remain applicable within the homogeneous roughness framework. The following analysis presents the aerodynamic roughness parameters assessed from direct drag together with mean velocity profile measurements which are spatially averaged over from 2 to 4 repeating units (depending on the case), to obtain statistically converged data. For the sake of clarity, only one mean and turbulence profile, from the sPIV data at matched Re_x ($Re_x \approx 4 \times 10^6$) is presented.

Two inner-normalised velocity profiles scaled with the friction velocity from the drag balance at the same Re_x for both surface configurations are presented in figure 3 and compared with a smooth-wall turbulent boundary layer profile from the DNS of Sillero et al (2013). The velocity profiles are shown to exhibit a substantial shift in the vertical axis indicative of the momentum loss caused by the higher wall shear stress experienced by the flow in comparison with the smooth wall. Config 1 is observed to have a relatively larger downward shift in comparison with Config 2 despite having a similar free stream velocity. However, this is expected since the skin-friction coefficient of Config 1 is larger than that of Config 2.

The zero-plane displacement (d) and the roughness function (ΔU^+) which characterise the shift in the velocity profiles observed in figure 3 are obtained by assuming the log-law. The former is determined by taking the derivative of the logarithmic part of equation 1 with respect to y, whereas the latter is obtained by simply taking

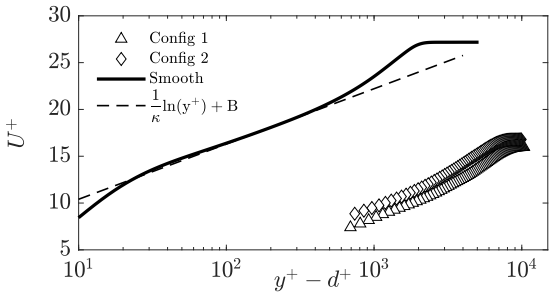

Fig. 3 Wall-normal distribution of the inner-normalised streamwise velocity profiles for both configurations at $Re_x \approx 4 \times 10^6$, compared with the DNS turbulent boundary layer smooth-wall of Sillero et al (2013). The dashed line represents the logarithmic distribution with the constants κ and B being 0.39 and 4.5 respectively.

the difference between the inner-normalised measured velocity profile and the log-law. These are expressed as

$$\Xi = \left(y^+ - d^+\right) \frac{dU^+}{dy^+} = \frac{1}{\kappa}, \tag{9}$$

and

$$\Psi = U^+ - \left(\frac{1}{\kappa}\ln(\mathrm{y}^+ - \mathrm{d}^+) + \mathrm{B} - \Delta\mathrm{U}^+\right). \tag{10}$$

Equation 9 is traditionally employed as a means to infer the logarithmic slope (Von-Kármán constant κ) and to provide a conservative indication of the log region; thus Ξ is generally referred to as the *indicator function* (Österlund et al, 2000). Consequently, by assuming κ to be universal between smooth- and rough walls, d can be determined by measuring the velocity gradient and the friction velocity (as done in this study). The zero-plane displacement is found as the value that minimises the difference between the left-hand-side (Ξ) and the right-hand-side ($1/\kappa$) of equation 9. The results shown in figure 4(a) indicate that the best solution that minimises this difference (the value of d^+ that yields $\Xi \approx 1/\kappa$) occurs around 0.15δ, leading to a good collapse of both profiles.

The results have shown that the values of d have a degree of scatter, however, this is believed to be caused by the uncertainty in locating the wall-normal origin due to the nature of these rough surfaces. The average zero-plane displacement as a fraction of the maximum roughness height $\overline{d}/k_p = 0.28$ and 0.57 for Config 1 and Config 2, respectively. Nonetheless, the variability in d was shown to have only a marginal influence on the roughness function. For instance, there is only a 1% change in ΔU^+ if the value of d is to be fixed at $d = k_p/2$, compared to the values returned from the fit described in equation 9. The roughness function ΔU^+ is subsequently determined by examining the Ψ profiles. Figure 4(b) presents the profiles of both surfaces and the results show the optimum fit solution that returns the best plateau occurs within the overlap region (highlighted grey region) $2k_p < \Psi_{fit} < 0.2\delta$. The profiles are also compared with the smooth-wall DNS data of Sillero et al (2013) and the figure clearly indicates that the rough profiles have a weaker wake region. In fact, the wake strength parameter can be deduced through the modified-log function Ψ, which quantifies the maximum departure from the logarithmic behaviour; $\Pi = \kappa/2 \times \max(\Psi)$. This method is sometimes favoured as it circumvents the use of a particular function. This also means that it can easily be inferred that the weaker the maximum value of Ψ gets, the weaker the wake strength parameter becomes.

With the roughness function values as a function of Reynolds number known, the equivalent sand-grain roughness height can be deduced using the fully-rough relation (equation 7). The variation of ΔU^+ with k_s^+ obtained from direct drag and velocity measurements is shown in figure 5(a) for both configurations. As expected, the data is shown to line up very well with the fully-rough asymptote already hinted at from the $C_f(Re_x)$ plot. The determined values of k_s are reported to be 11.6 mm and 8.05 mm, corresponding to $1.85k_p$ and $1.28k_p$ for Config 1 and Config 2, respectively. As fractions of the boundary layer thickness, they represent 10.3% and 7.4% for Config 1 and Config 2, respectively. These values are seen to be lower than those reported by direct drag measurements and using equation 6, indicating that $k_{s,DB}$ overestimates the roughness lengthscale by as much as 38%. Using these values, the inner-normalised mean velocity profiles can be re-plotted against the wall-normal distance normalised by k_s as depicted in figure 5(b).

The results exhibit a good collapse of the two configurations within a range of $1 < (y-d)/k_s < 2$ corresponding to the overlap region where ΔU^+ was estimated. They are observed to follow a

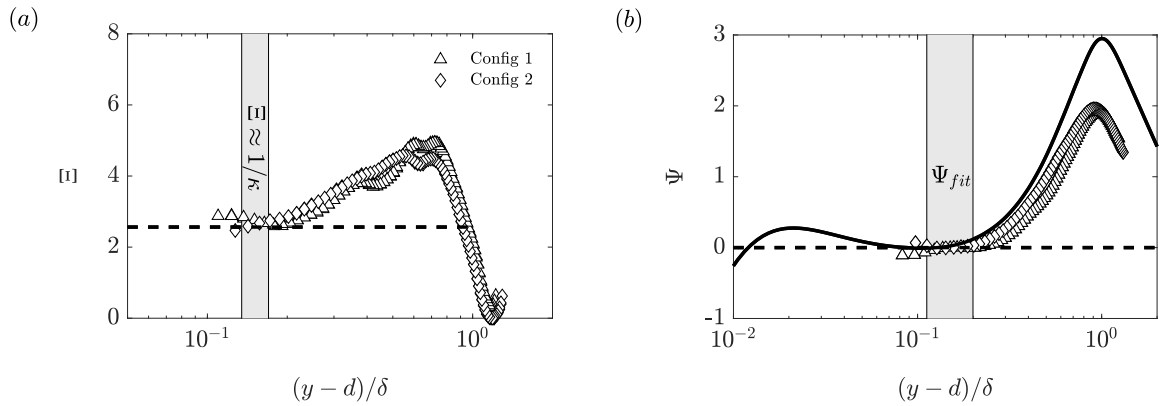

Fig. 4 (*a*) Profiles of the variation of the indicator function Ξ determined using a second-order central-difference scheme, with the highlighted region indicating the plateau where $\Xi \approx 1/\kappa$. (*b*) Profiles of the modified log-law function Ψ for both configurations, compared with the DNS turbulent boundary layer smooth-wall of Sillero et al (2013). The shaded region highlights the boundaries where the roughness function ΔU^+.

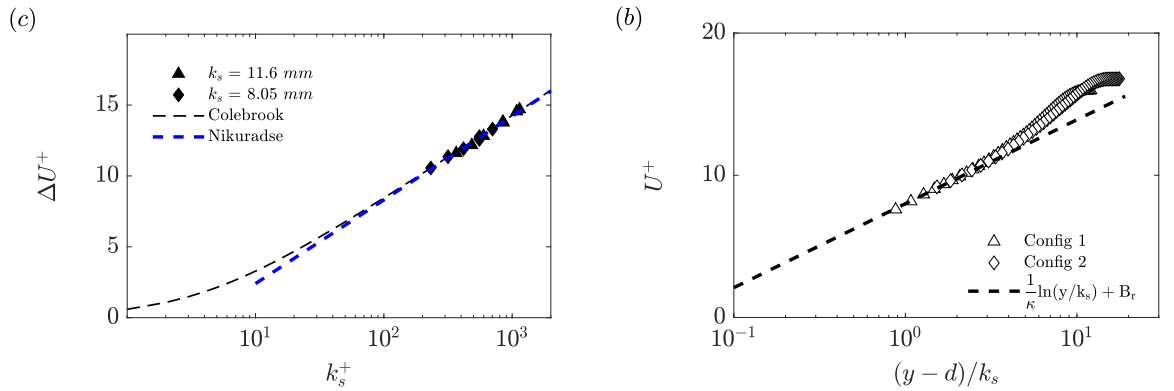

Fig. 5 (*a*) Variation of the roughness function ΔU^+ against k_s^+ for two configurations determined from the direct drag measurements and velocity profiles. (*b*) Inner-normalised streamwise velocity profile with wall-normal distance normalised by k_s. The additive constant $B_r = B + C \approx 8$ for this data.

logarithmic behaviour represented by the black-dashed line, with a fully rough intercept $B_r \approx 8$, as opposed to the classically reported 8.5. It should be recalled that the latter value is derived from pipe flow data. In fact, the logarithmic slope κ for boundary layers (currently taken as 0.39) is smaller than that observed in pipe flows, generally reported as being 0.41 (Marusic et al, 2013), hence the associated intercept B_r being lower to the generally used value in pipes and channel flows. It is worth noting that the selected value for C remains applicable to boundary layers, as evidenced by the current intercepts for both smooth- and rough-walls, calculated as $B_r - B = 8 - 4.5 = 3.5 = C$. The profiles are also shown to have a weaker departure from the logarithmic distribution in the outer region, but this is perhaps clearer when comparing the Ψ profiles with respect to the smooth wall as presented in figure 4(*b*).

Using the values of k_s obtained from the profiles and drag-balance, we can also predict the change in Π^R. This prediction can subsequently be checked against the value of Π^R determined directly from the velocity profile data. Using equation 7 together with 5 and 6 at matched values of δ^+, it can be shown that:

$$\Pi^R = \Pi^S + \frac{1}{2}\ln\left(\frac{k_s}{k_{sDB}}\right). \tag{11}$$

With the values of k_s and k_{sDB}, the average values of Π^R are predicted to be 0.41 for both Config 1 and Config 2, respectively, as shown in figure

6(a) as blue-dashed lines. This prediction confirms the profiles are expected to have a weaker wake parameter in comparison with the smooth wall.

To examine Π^R, it is possible to use either formulation of the velocity profiles expressed by equations 1 or 2. Although different analytical expressions for W yield different values of Π (as stated in the introduction), the conclusion drawn in the current study remains unchanged when employing alternative expressions. Therefore, instead of using an analytical expression, equation 3 is currently preferred as it directly quantifies Π^R without the need for a fit, thus eliminating additional fitting uncertainties. Rearranging the terms in equation 3 yields the expression,

$$\Pi^R = \frac{1}{2}\left[\kappa(U_\infty^+ + \Delta U^+ - B) - \ln(\delta^+)\right]. \quad (12)$$

Π^R is subsequently determined directly given all quantities $(U_\infty^+ + \Delta U^+ - B)$ have been measured. The results of the wake strength parameter with respect to Reynolds number are depicted in 6(a) together with the prediction (blue line) showing the values to be substantially lower than that of a smooth-wall of $\Pi \approx 0.57$ (determined using Sillero et al (2013) DNS smooth-wall data). Despite the scatter in the results, both surfaces are shown to yield relatively similar mean values ranging between 0.38–0.44 (across the different speeds and cases), with an average value of 0.41 nearly a 30% reduction in wake strength. In hindsight, these results provide an explanation for the higher values observed in ΔU_{DB}^+ (hence $k_{s,DB}$) obtained using drag information with the assumption of outer-layer similarity without prior knowledge of the flow behaviour. Examining equations 5 and 6 shows this difference can only be attributed to differences in the value of Π between smooth and rough walls. This would suggest that velocity profiles would not follow universal outer-layer similarity.

Additionally, the values of Π^R determined from equation 11 are shown to be in agreement with the ones measured from the profiles. The latter is shown to have a degree of variability ($\pm 5\%$) but this is expected given the change in Reynolds number. The values of Π^R are also reported in table 4 alongside other relevant aerodynamic parameters for both configurations. The similarity in Π^R for Config 1 and Config 2 despite their difference in δ/k_s reveals that perhaps outer-layer similarity between Config 1 and Config 2 can still be valid.

In a similar fashion to Figure 3 presented by Squire et al (2016), figure 6(b) presents the current data in the $(\delta/k_s, k_s^+)$-plane along with data from other rough-wall turbulent boundary layer experiments; the sand-grain roughness and woven mesh of Flack et al (2007), the sand-grain roughness of Squire et al (2016) and the urban roughness of Ferreira and Ganapathisubramani (2021), with the latter being performed in the same facility as in the current study. The horizontal axis reflects the ratio of the aerodynamic roughness to the viscous length scales and is generally indicative of the flow regime (i.e. fully-rough regime for $k_s^+ > 100$, aerodynamically-smooth for $k_s^+ < 6$ and transitionally-rough regime in between). On the other hand, the vertical axis indicates a scale separation between the boundary layer thickness and the aerodynamic roughness height equivalent to the friction to roughness Reynolds numbers ratio ($\delta/k_s \equiv \delta^+/k_s^+$).

In this example, the plane is divided into four quadrants delineating regions of; mild roughness in transitionally-rough regime (Q_1 with $\delta/k_s > 10$ and $k_s^+ < 100$), mild roughness in fully-rough regime (Q_2 with $\delta/k_s > 10$ and $k_s^+ > 100$), strong roughness in fully-rough regime (Q_3 with $\delta/k_s < 10$ and $k_s^+ > 100$) and finally strong roughness in transitionally-rough regime (Q_4 with $\delta/k_s < 10$ and $k_s^+ < 100$). According to this chart, the current roughness seems to generate a relatively strong aerodynamic roughness length-scale compared with the P36-sand-grain roughness tested by Squire et al (2016). It instead compares well with the medium-mesh and P24-sand-grain cases examined by Flack et al (2007) but remains weaker than the cube roughness generally used to model urban roughness as demonstrated by Ferreira and Ganapathisubramani (2021).

As stated in the introduction, the outer-layer similarity hypothesis implies that the roughness sublayer confines itself to the inner region while a large portion of the flow remains unaffected by the surface condition. To assess the validity of this hypothesis, the mean velocity deficit along with the streamwise turbulence intensity profiles are examined in the wake region (which

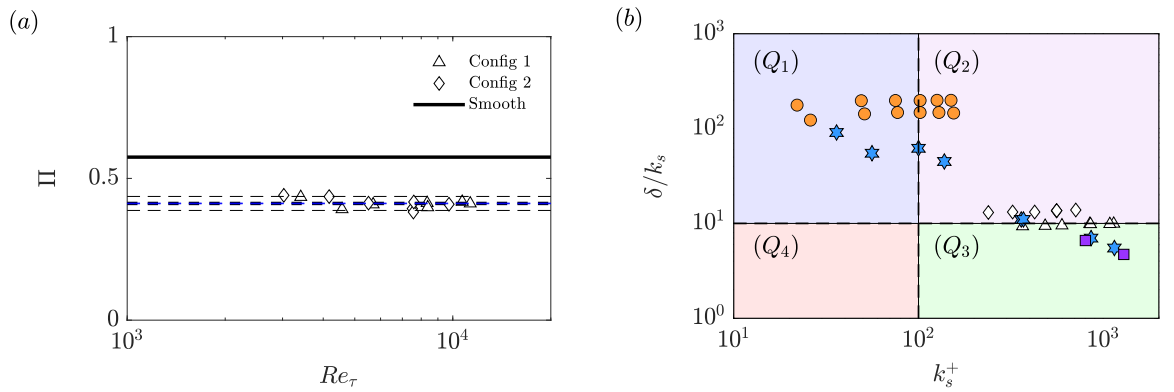

Fig. 6 (a) Variation of the wake strength parameter Π^R with respect to the friction Reynolds number Re_τ (δ^+) estimated from the composite profile, compared with the smooth-wall Π^S (solid black line) and the predicted Π^R (dashed blue lines) using equation 11. Π^S is determined from the DNS smooth-wall profile of Sillero et al (2013). (b) Comparison of the results with rough-wall data reported in the literature which supports the outer-layer similarity hypothesis shown in the $(\delta/k_s, k_s^+)$-plane. Blue stars: Flack et al (2007). Orange circles: Squire et al (2016). Purple squares: Ferreira et al (2018). White diamonds and triangles: current data.

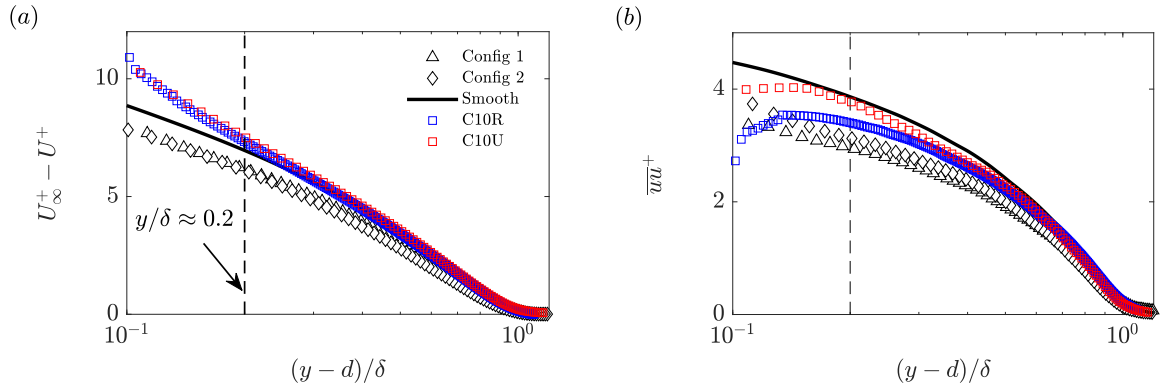

Fig. 7 (a) Wall-normal distribution of the velocity profiles in defect form for both configurations. (b) Variation of the inner-normalised streamwise turbulence intensity profiles. The black solid line in both figures represents the DNS smooth-wall data from Sillero et al (2013). The profiles are also compared with the fully-rough profiles (C10R and C10U) from Ferreira and Ganapathisubramani (2021) measured in the same facility. The turbulence intensity profiles have been corrected using the method proposed by Lee et al (2016) to account for the energy attenuation due to the filtering that resulted from the PIV spatial resolution.

nearly represents the upper 80% of the boundary layer). The results from both configurations are illustrated in figure 7(a) and (b), and compared with their equivalent smooth-wall profiles from Sillero et al (2013). It should be noted that despite the unmatched δ^+'s of the different profiles (the DNS date has a friction Reynolds number of $\delta^+ \approx 2000$), the wake region is only weakly dependent on Reynolds number, hence the comparison remains valid. The results presented in figure 7(a) clearly show the absence of similarity between the smooth- and rough-wall profiles, with current profiles presenting a smaller deficit compared with the smooth wall (solid line). The lack of similarity extends almost up to 0.7 –0.8 δ, which represents nearly $7k_s$ and $10k_s$ for Config 1 and 2 respectively.

The figure also compares the current results with rough-wall profiles from surfaces made of regularly distributed cubes with random (C10R) and uniform (C10U) heights, examined by Ferreira et al (2018) within the same facility. These types of surfaces are commonly utilised to model urban flows and have been widely documented in the literature (Castro, 2007; Amir and Castro, 2011; Castro et al, 2013). Both cube rough surfaces yield different behaviours in the outer flow in comparison with the biofouled surfaces. In fact,

these surfaces maintain a good degree of similarity (in the mean flow) with the smooth-wall flow for $y/\delta > 0.2$, with a wake strength parameter of $\Pi \approx 0.42$ and 0.51 for C10R and C10U respectively. These are associated with a $\delta/k_s \approx 5$ and 7 for C10R and C10U, which can be considered a relatively stronger roughness than the current ones, also seen in the $(\delta/k_s, k_s^+)$-plane of figure 6(*b*).

Moreover, the blockage due to roughness in both experiments is also similar meaning their corresponding acceleration parameters are very similar. This suggests that the absence of outer-layer similarity cannot be attributed to a small value of δ/k_s, nor to the weaker value in the wake strength parameter alone (if caused by a favourable pressure gradient). However, their influences cannot be fully ignored.

Figure 7(*b*) shows the inner-normalised streamwise turbulence intensity profiles also compared with the smooth-wall profile. These profiles have been corrected to account for the energy attenuation caused by the filtering of the sub-resolution scales in the PIV measurements, using the method outlined by Lee et al (2016). It is seen that the turbulence intensities have only been very marginally affected in the outer region (less than 1% attenuation in the outer region. Overall, the results clearly indicate that the turbulence intensities have a smaller magnitude in comparison with their equivalent smooth-wall profile. This observation reveals that the increase in frictional drag caused by the roughness is not systematically accompanied by a proportional increase in the turbulence intensity, as evidenced by the absence of outer-layer similarity.

3.3 Method 3 and 4: OLS and CSS

In the absence of drag balance measurements, U_τ has to be indirectly determined and then used to obtain ΔU^+, k_s, and Π. As opposed to direct methods, indirect methods essentially rely on mean and turbulence flow assumptions to infer the wall shear stress. For example, Clauser chart method (Clauser, 1956) is widely used to infer U_τ in smooth-walls, while its modified version applied to rough-walls (Perry and Li, 1990), determines U_τ, ΔU^+ and d altogether from the log region for a given κ and B. Alternatively, U_τ can be determined from the total shear stress method, which assumes a constant shear stress layer in the overlap region to exist, assumed to be equal to the wall shear stress (Schultz and Flack, 2005). Other methods rely on the flow's streamwise growth, such as the Von-Kármán momentum integral method. In this work, two methods at two ends of complexity are evaluated: 1) assumption of outer-layer similarity for streamwise mean and turbulence intensity (Townsend, 1976) and 2) comprehensive shear-stress method recently proposed by Womack et al (2019). Results from both methods are presented in the following and compared to the direct measurement results.

Assuming the validity of the outer-layer similarity hypothesis implies that both functions f and g_{ij} in equation 4 are universal for the smooth- and rough-wall flows. This is clearly not the case for both currently investigated surfaces, however, it is important to know the effect of this assumption as this method has been previously employed to determine full-scale frictional drag and predict the drag penalty of ships at high Reynolds numbers (Monty et al, 2016). Forcing collapse of profiles is achieved by simultaneously minimising the difference in both velocity deficit and turbulence intensity between the smooth- and rough-wall data in the outer region ($y > 0.2\delta$). This results in a new U_τ value which is subsequently used to evaluate ΔU^+ from the new inner-scaled profiles, for which an appropriate k_s is determined using equation 7.

In the second method, the aerodynamic parameters are estimated using the comprehensive shear-stress method proposed by Womack et al (2019). This method builds on the procedure initially outlined by Volino and Schultz (2018) and follows an iterative error minimisation procedure to determine U_τ, d, y_0 (equivalent to ΔU^+ or k_s^+) and Π using integral momentum equations - total shear stress balance together with the law-of-the-wall. Womack et al (2019) demonstrated by using a single streamwise velocity and a Reynolds shear stress profile, U_τ can be retrieved to within $\pm 1-4\%$ when compared with direct drag measurements. To allow a consistent comparison between the direct method and this indirect method, the fitting region adopted for the log-law is similar to the previously used, $2k_p \approx 0.1 < y/\delta < 0.2$. For the Reynolds shear stress profiles, the optimisation was carried out within a range of $0.2 < y/\delta <$

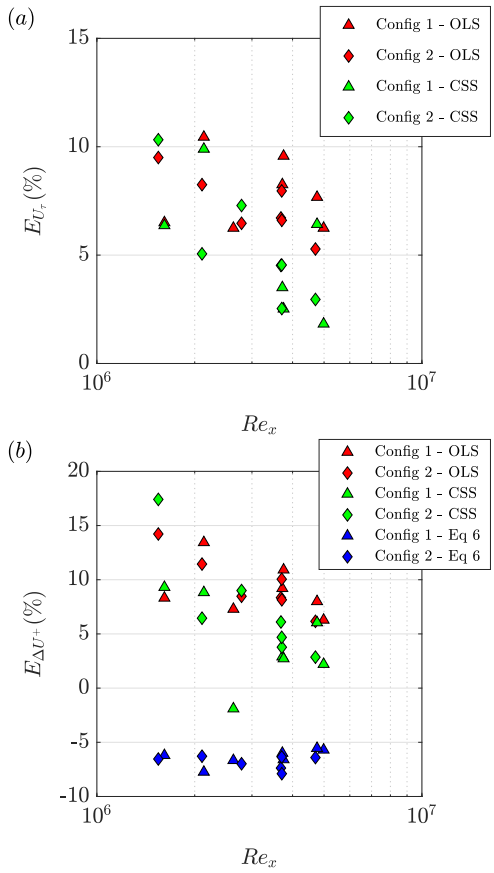

Fig. 8 (*a*) Percentage in the relative difference of the friction velocity ($E_{U_\tau}(\%) = (U_\tau - U_{\tau,indirect})/U_\tau$) obtained from the two indirect methods (OLS and CSS) with respect to the direct measures from the drag balance. (*b*) Percentage in the relative difference of the roughness function ($E_{\Delta U^+}(\%) = (\Delta U^+ - \Delta U^+_{indirect})/\Delta U^+$) obtained from the three indirect methods (OLS and CSS in addition with using equation 6) compared with the measures using $U_{\tau,DB}$ and the log-law profile

.

0.3. The interactive graphical user interface software made available by Womack et al (2019) was used to carry out this analysis.

Results of the aerodynamic parameters from the different methods are presented in table 4, and their differences are illustrated in figure 8 for both configurations. Figure 8(*a*) compares the percentage in the relative difference of the friction velocity ($E_{U_\tau}(\%) = (U_\tau - U_{\tau,indirect})/U_\tau$) obtained from the two indirect methods (OLS and CSS) with the measures from the drag balance. Despite the noticeable scatter, the results indicate that in both methods, U_τ is underestimated for both configurations. The CSS method is shown to give consistently relatively better results as the Reynolds number increases, with the difference reaching less than 3%, which falls within the accuracy range results provided by Womack et al (2019). On the other hand, the OLS method is shown to underpredict the friction velocity by over 10% at low speeds then the difference reduces nearly to 5% as the speed increases.

The relative difference in estimating the roughness function ($E_{\Delta U^+}(\%) = (\Delta U^+ - \Delta U^+_{indirect})/\Delta U^+$) is shown in figure 8(*b*) and compares the three different methods; OLS, CSS and equation 6 (which uses direct drag measurements but assumes $\Pi^S = \Pi^R$), against the log-law method which is expected to be the most accurate method (since it uses U_τ measured with the drag balance without any mean and turbulence flow assumptions). It is clear from this figure that equation 6 overestimates the roughness function when compared with the correct ΔU^+, while the other indirect methods tend to underestimate the value of ΔU^+.

Similarly to the degree of scatter observed in figure 8(*a*), the relative difference in the roughness function shown in figure 8(*b*) seems to reduce as the Reynolds number increases. Nonetheless, these differences are enough to cause a considerable underestimation in k_s as shown in table 4, with $k_{s,OLS}$ and $k_{s,CSS}$ underpredicting k_s by 32% and 15% for Config 1 and 31% and 23% for Config 2, respectively. Hence, this could have an important effect when predicting the drag penalty at higher Reynolds numbers.

It is shown in table 4 that the OLS method results in a wake strength parameter value of roughly 0.48 which is relatively larger than the previous estimate, however, remains about 15% smaller than the smooth-wall Π^S of 0.57. This is believed to result from the absence of a complete simultaneous collapse when imposing similarity in the mean and turbulence statistics, but also due to subtle differences in the shape of the wake region itself. This behaviour is also observed in the C10R and C10U profiles, in which, despite the relatively good collapse of the mean profiles with the smooth-wall data, the overlap region remains noticeably deviated from that of the smooth wall. For the CSS methods, the wake strength parameter showed a degree of scatter across different speeds. However, this is inherently related to the

way Π is determined, since Womack et al (2019) defined it as the wake's maximum departure from the extrapolated log-law, to avoid assuming a universal wake function.

Figure 9 illustrates the different results in using indirect methods in estimating C_f in these laboratory-scale surfaces. Estimates of the skin-friction coefficient from both OLS and CSS methods, compared with the direct drag measurements are exemplified for Config 2. The results clearly show that both methods underpredict C_f, with the CSS method underestimating C_f by close to 6% at the highest Reynolds number, as opposed to 10% when assuming the outer-layer similarity hypothesis.

3.4 Drag penalty predictions

Now that direct and indirect methods have been assessed, a prediction of the spatially-averaged frictional drag C_F at high Reynolds numbers Re_x (with fixed U_∞ and ν but increasing x) can be made through each method. To this end, the procedure proposed by Monty et al (2016) is employed. It is an integral boundary layer evolution method based on numerical integration of the skin friction over a given length of the developing flow, assuming a velocity profile composed of a logarithmic and wake region (see Monty et al (2016) for more details). The profile can be fully described by its freestream velocity U_∞, kinematic viscosity ν, and wake strength parameter Π along the equivalent sand-grain roughness height k_s. For the sake of consistency with the above analysis, the logarithmic region uses a $\kappa = 0.39$ and $B = 4.5$.

Figure 10 shows the variation of C_F as a function Re_L, highlighting full-scale predictions for each method (colour-coded curves) and depicting the influence of the wake strength parameter (dashed curves). The graph is shown for Config 2, but the same behaviour is also observed for Config 1. This figure is obtained for a unit Reynolds number $U_\infty/\nu \approx 2 \times 10^7$. The results show that the relative change in frictional drag with respect to the smooth-wall ($\Delta C_{F,s} = (C_F - C_{F,s})/C_{F,s}$, with $C_{F,s}$ being the smooth-wall frictional drag) is over 230% at a Reynolds number of $Re_x \approx 10^9$ (typical of a Reynolds number of a 50 m long vessel) when using the direct method (k_s, Π^R). This relatively large value in $\Delta C_{F,s}$ is not unexpected as according to Schultz (2007), the equivalent sand-grain roughness of the current surface should be regarded as heavy calcareous fouling ($k_s \sim O(10)$ mm). Similarly, the same result can be achieved when using $k_{s,DB}$ and Π^S as shown by the relatively good collapse of both predictions (solid black and blue curves). The reason for this is trivial and is explained by equation 11 which shows that the overestimated value in $k_{s,DB}$ is compensated for by the assumption of Π^S. Hence, the skin friction prediction using $(k_{s,DB}, \Pi^S)$ is similar to using (k_s, Π^R).

Furthermore, it's worth noting that both indirect methods, OLS and CSS, tend to provide underestimated values for C_F; however, the CSS method shows relatively better accuracy. On the other hand, the assumption of $\Pi = \Pi^S$ clearly shows that the drag is systematically underpredicted. To highlight these differences, three different fetch Reynolds numbers have been selected for comparison as seen in figure 10 (vertical dashed lines). At $Re_L = 10^8$, the prediction using $(k_{s,DB}, \Pi^S)$ overestimated the predicted value by less than 1.5%, whereas using (k_s, Π^S) the prediction worsens to 6–7% below the direct prediction. As observed from the graph, the substantial undervaluation scenario occurs if the outer-layer similarity hypothesis is assumed even at these high Reynolds numbers, as this results in a drag underprediction of around 14–15%. On the other hand, the CSS is seen to give relatively better predictions with underestimates around 6–7% when using Π^R but worsen to over 11–12% when using a Π^S.

These different estimates remain consistent with increasing Reynolds numbers, albeit with a clear tendency of reduction in the relative difference due to the asymptotic nature of the frictional drag at very high Reynolds numbers. This can be explained by the fact that at very high Reynolds numbers, most of the drag is expected to be captured by the logarithmic region which increases proportionally with Re_L, while the wake region (hence changes in Π) will have a proportionally lesser impact as observed. Quantitative figures are provided in table 5 for both configurations, summarising the influence of using the different methods on drag prediction.

Nevertheless, it is important for the reader to be cautious when interpreting these relative differences, as they are specific to the particular roughness under investigation. In fact, other rough

Table 4 Aerodynamic parameters determined from four different methods namely; method 1 using $U_{\tau,DB}$ and equation 6, method 2 using $U_{\tau,DB}$ and log-law profile, method 3 using outer-layer similarity hypothesis, and method 4 using the comprehensive shear stress method of Womack et al (2019), respectively. The estimates of the equivalent sand-grain roughness height from the different methods for Config 1 are: $k_{s,DB} = 16.11$ mm, $k_s = 11.59$ mm, $k_{s,OLS} = 7.88$ mm and $k_{s,CSS} = 9.76$ mm associated with the methods 1, 2, 3 and 4, respectively. The results for Config 2 are: $k_{s,DB} = 11.13$ mm, $k_s = 8.05$ mm, $k_{s,OLS} = 5.56$ mm and $k_{s,CSS} = 6.13$ mm associated with the methods 1, 2, 3 and 4, respectively.

Case	U_∞ (m/s)	Method 1 DB				Method 2 direct				Method 3 OLS				Method 4 CSS			
		U_τ	k_s^+	Π	δ^+	U_τ	k_s^+	Π	δ^+	U_τ	k_s^+	Π	δ^+	U_τ	k_s^+	Π	δ^+
Config 1	7.76	0.49	336	0.43	3412	0.49	508	0.57	3412	0.45	232	0.49	3190	0.45	288	0.46	3195
	10.29	0.65	485	0.39	4570	0.65	674	0.57	4570	0.57	295	0.49	4092	0.58	367	0.55	4118
	12.75	0.80	598	0.41	5694	0.80	831	0.57	5694	0.75	381	0.46	5338	0.80	506	0.41	5735
	18.05	1.13	846	0.41	8342	1.13	1175	0.57	8342	1.04	527	0.48	7654	1.09	686	0.44	8050
	23.07	1.45	1086	0.41	10689	1.45	1509	0.57	10689	1.34	681	0.48	9869	1.36	855	0.47	10000
	23.82	1.50	1140	0.41	11312	1.50	1584	0.57	11312	1.41	726	0.47	10605	1.47	942	0.41	11105
	18.25	1.14	853	0.39	8374	1.14	1185	0.57	8374	1.03	524	0.48	7573	1.11	700	0.40	8163
Config 2	7.61	0.45	232	0.44	3027	0.45	321	0.57	3027	0.41	145	0.54	2739	0.40	158	0.5	2714
	10.35	0.62	316	0.43	4172	0.62	437	0.57	4172	0.56	200	0.52	3828	0.58	228	0.47	3961
	13.70	0.82	417	0.41	5510	0.82	577	0.57	5510	0.76	269	0.47	5153	0.75	295	0.48	5108
	18.09	1.08	552	0.39	7513	1.08	764	0.57	7513	1.01	356	0.46	7008	1.03	401	0.41	7173
	23.06	1.37	702	0.41	9734	1.37	972	0.57	9734	1.30	459	0.46	9220	1.33	519	0.43	9447
	18.07	1.08	555	0.38	7567	1.08	769	0.57	7567	1.01	358	0.45	7067	1.05	412	0.39	7375
	18.15	1.08	555	0.41	7590	1.08	768	0.57	7590	0.99	353	0.49	6985	1.03	404	0.45	7245

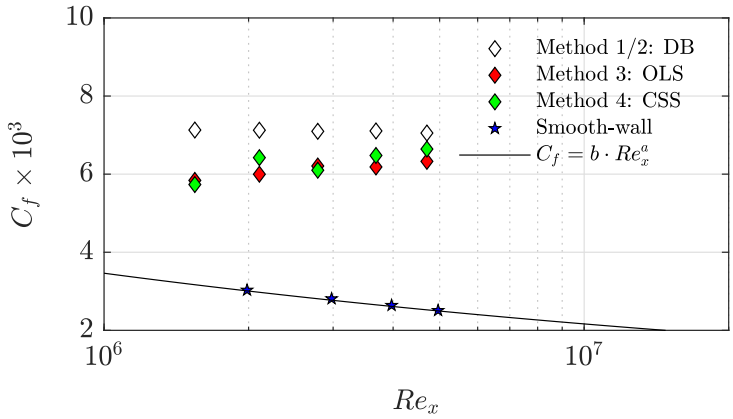

Fig. 9 Comparison of the skin-friction coefficient determined from the indirect methods with the estimates from the drag balance for Config 2.

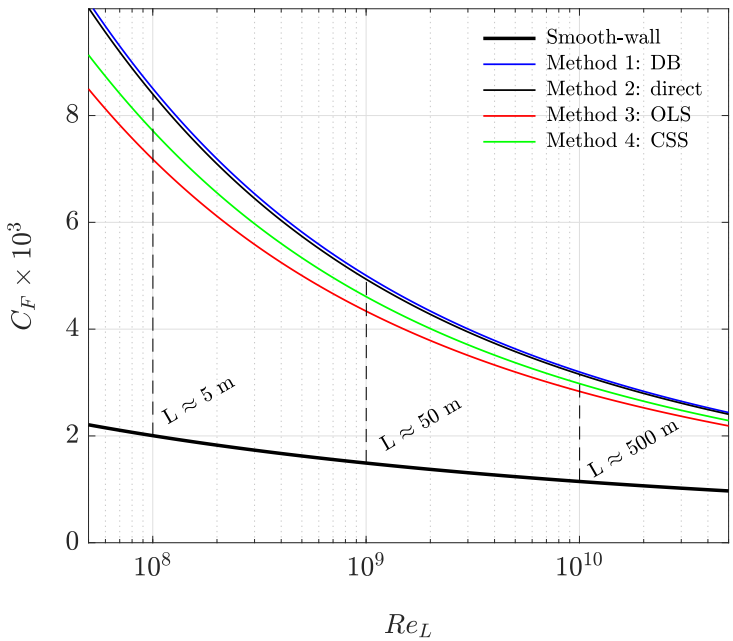

Fig. 10 Comparison between the different methods of the predicted full-scale average skin-friction coefficient C_F as a function of the fetch Reynolds number Re_L using the procedure presented by Monty et al (2016) for Config 2. The used unit Reynolds number is $U_\infty/\nu \approx 2 \times 10^7$with $U_\infty \approx 18$ ms^{-1} and $\nu \approx 9 \times 10^{-7}$ m^{2}s^{-1}.

surfaces will likely produce different values. This was observed after carrying out the same analysis described in section 3.3 on the surfaces examined by Ferreira et al (2018). The results showed that the OLS and CSS method only underpredicted the value of C_F by roughly 3% at the highest Reynolds number. Therefore, the OLS and CSS methods remain potentially excellent alternatives to assess the aerodynamic roughness parameters and predict the drag penalty at high Reynolds numbers over a wide range of rough surfaces, when direct drag measurements are not available (Monty et al, 2016; Womack et al, 2019). It is also recalled that these predictions are only valid for flat surfaces, without pressure gradients, and care should be taken when interpreting these results for practical engineering applications (e.g. flows under favourable and/or adverse pressure gradients due to surface curvatures).

Table 5 Assessment of the relative difference in predicting the drag penalty using the different methods, at three different Reynolds numbers Re_L for both biofouled roughness configurations. The relative difference is expressed as percentage with $E_{C_{F,m}}(\%) = (C_{F,m} - C_F)/C_{F.m}$, with C_F and $C_{F,m}$ representing the direct and indirect methods, respectively.

		$E_{C_{F,m}}(\%)$				
Case	Re_L	Method 1 $(k_{s,DB}, \Pi^S)$	Method 2 (k_s, Π^S)	Method 3 $(k_{s,OLS}, \Pi^S)$	Method 4 $(k_{s,CSS}, \Pi^R)$	Method 4 $(k_{s,CSS}, \Pi^S)$
Config 1	10^8	-1.06	7.60	15.67	6.33	11.15
	10^9	-1.41	5.60	12.89	4.93	8.93
	10^{10}	-1.40	4.46	10.75	4.09	7.31
Config 2	10^8	-1.28	6.47	14.34	7.74	12.44
	10^9	-1.45	5.21	12.09	6.51	10.33
	10^{10}	-1.41	4.20	10.14	5.48	8.62

Finally, it is essential to keep in mind that the above analysis predicts drag within the classical framework of homogeneous roughness. However, in practical applications, this tool does not account for the inherent patchiness or heterogeneity found in several real-world applications. The lack of comprehensive data on this topic poses significant challenges for our current predictive framework, as noted by Chung et al (2021). This limitation primarily stems from our limited understanding of the drag behaviour over heterogeneous rough surfaces (Medjnoun et al, 2018, 2020). In their recent work, Hutchins et al (2023) have proposed a power-mean approach for defining an equivalent homogeneous roughness length that takes into account patchiness or the heterogeneous distribution of roughness on ship hulls. This approach seems promising, especially when dealing with patch sizes significantly larger than the boundary layer thickness. It has the potential to address some challenges posed by heterogeneous roughness, however, its application in existing full-scale drag prediction methods highlights the need for further investigations in this field. Obtaining high-fidelity data across a broad range of Reynolds numbers is particularly crucial in advancing our understanding of this complex problem.

4 Conclusions

A turbulent boundary-layer flow over two configurations of a realistic biofouled rough surface scanned, scaled and replicated from a ship hull is experimentally investigated. Detailed laboratory wind-tunnel experiments have been carried out, which consisted of direct drag measurements using an in-house floating element drag balance together with PIV to assess the flow field.

Data from direct drag measurements revealed that the skin-friction coefficient reached the fully-rough regime under both surface configurations, shown by the invariance of C_f with respect to the Reynolds number. In these laboratory-scale surfaces, the frictional drag is shown to exceed 300% that of a smooth wall at matched Re_x. Using this information along with velocity measurements, limitations of similarity laws have been discussed. When considering only direct drag and boundary layer thickness data, it becomes evident that the aerodynamic roughness lengthscale tends to overestimate the actual value, sometimes by as much as 40%. This overestimation is shown to be caused by the reduction in the wake strength parameter, which itself is shown to be 30% weaker than that of a smooth wall.

Lack of outer-layer similarity in both mean flow and turbulence intensities is reported, despite following the classically admitted conditions ($\delta^+ > 3000$, $k_s^+ > 200$ and $k_s/\delta \approx 0.1$). Although

flow fields were not shown for brevity, the mean and turbulent structures remain generally unperturbed in the outer region, with an excellent degree of spanwise homogeneity. The canopy layer harboured intense shear layer regions generated by the barnacles which seemed to propagate towards the outer layer, albeit confined below $y/\delta < 0.15$. This means that the lack of universal outer-layer similarity can potentially be caused by the generation of roughness-scale structures that emanate from the barnacles, leading to changes in the uniform momentum zones and the wake intermittent activity resulting in a weaker wake parameter.

By assuming the validity of the outer-layer similarity hypothesis and using the comprehensive shear stress (Womack et al, 2019) methods, indirect estimates of the aerodynamic parameters have been obtained and compared with results from the direct measurements. The comparison highlighted the limitation of using these flow assumptions, which resulted in underrating the equivalent sand-grain roughness on average for both configurations by over 30% and 20% for the OLS and CSS methods, respectively. Using the integral boundary layer evolution method outlined by Monty et al (2016) results from the different indirect methods have been used to assess the frictional drag penalty at high Reynolds and contrasted with the predictions from direct measurements.

The current results also showed that accurate prediction of skin friction remains possible using an indirect estimate of the roughness function ΔU^+_{DB}, provided direct drag measurements at laboratory-scale data are available. In fact, for a nominally zero-pressure gradient turbulent boundary layer developing over a flat surface, $k_{s,DB}$ (obtained from direct drag measurements) together with a wake strength parameter $\Pi = \Pi^S$ result in a similar frictional drag prediction as when using directly measured estimates of k_s and Π^R. However, when indirect drag estimates are used to characterise the roughness, frictional drag predictions at high Reynolds numbers can be underestimated. At a Reynolds number of $Re_x \approx 10^9$ (equivalent to a Reynolds number of a 50 m long vessel at full-speed), assuming outer-layer similarity underestimated the frictional drag by over 12% while the comprehensive shear stress method resulted in approximately 6% difference. However, as the Reynolds number increases the differences become smaller since the inner layer contributes substantially to the momentum deficit, and "erroneous" outer-layer information does not substantially affect the predictions.

Finally, in spite of highlighting the importance of using a direct method to assess drag as opposed to relying on indirect techniques, it is necessary to recall that the quantitative results of the indirect methods analyses and their predictions of drag penalty at high Reynolds numbers remain tied to the surfaces investigated in this study. The fact that the analysis of both surfaces showed different rates of drag penalty predictions (see table 5) means that other surfaces will likely produce other figures and in some situations, OLS and CSS methods will remain excellent options to assess the aerodynamic roughness parameters and predict the drag at high Reynolds numbers when direct drag measurements are not available (Monty et al, 2016; Womack et al, 2019).

Appendix

Uncertainty analysis

Although the experiments are conducted in a well-controlled environment, measurements are inherently contaminated by a degree of uncertainty. There are several sources of uncertainties but these are generally divided into two categories; *i*) systematic errors (associated with the accuracy of the measurement system), and *ii*) random errors (linked to the precision of the measured quantity). In this section, we provide a quantification of the main sources of errors that contribute to the uncertainty in the assessment of the aerodynamic roughness parameters, to help in the interpretation of the drag penalty predictions at high Reynolds numbers. The uncertainty estimates reported below are calculated using the method of Moffat (1988) with a 95% confidence bound.

The wall-shear stress (hence the friction velocity and skin-friction coefficient) has been determined using the method presented by Ferreira et al (2018). In that study, Ferreira et al (2018) have shown that the dominant sources of uncertainty stem from the calibration and the method used to infer the wall-shear stress, and to a lesser

extent, the inclination of the floating element and the air properties. Using a linear uncertainty propagation, the combined (i.e. the accuracy and precision) uncertainty ϵ on the friction velocity and drag is shown to be $\epsilon_{U_\tau} \approx 2.32\%$ and $\epsilon_{C_f} \approx 4.66\%$ at the lowest speed (worst case), and reduces with increasing speed, as reported in table 6.

Table 6 Overall uncertainty estimates of the friction velocity ϵ_{U_τ} and skin-friction coefficient ϵ_{C_f} for both configurations, from the drag measurements using the floating-element drag balance.

Case	U_τ (ms^{-1})	$C_f \times 10^3$	ϵ_{U_τ} (%)	ϵ_{C_f} (%)
Config 1	0.59	7.85	2.04	4.13
	0.73	7.88	1.73	3.52
	0.86	7.86	1.91	3.89
	1.01	7.86	1.26	2.59
	1.14	7.87	0.81	1.63
	1.29	7.93	0.52	1.01
	1.43	7.91	0.45	0.86
	1.58	7.99	0.53	1.09
	1.72	8.02	0.74	1.48
Config 2	0.55	7.12	2.32	4.66
	0.69	7.12	1.95	3.92
	0.82	7.09	2.19	4.38
	0.95	7.11	1.69	3.30
	1.08	7.10	1.22	2.42
	1.22	7.09	0.84	1.68
	1.34	7.04	0.82	1.69
	1.48	7.09	0.73	1.48
	1.61	7.04	1.06	2.15

The uncertainty in the roughness function is deduced by applying a linear error propagation to equation 1, which is rewritten in its log-law form without the wake extension, as:

$$\Delta U^+ = \frac{1}{\kappa} \ln\left(y^+ - d^+\right) + B - U^+. \tag{13}$$

Assuming all quantities are uncorrelated, the combined uncertainty $\epsilon_{\Delta U^+}$ can be expressed as:

$$\begin{aligned}\epsilon^2_{\Delta U^+} &= \left(\frac{\partial \Delta U^+}{\partial \kappa}\right)^2 \epsilon^2_\kappa + \left(\frac{\partial \Delta U^+}{\partial y^+}\right)^2 \epsilon^2_{y^+} \\ &+ \left(\frac{\partial \Delta U^+}{\partial d^+}\right)^2 \epsilon^2_{d^+} + \left(\frac{\partial \Delta U^+}{\partial B}\right)^2 \epsilon^2_B \\ &+ \left(\frac{\partial \Delta U^+}{\partial U^+}\right)^2 \epsilon^2_{U^+} + \epsilon^2_{\Delta U^+ fit} \\ &= \left(\frac{\ln(y^+ - d^+)}{\kappa^2}\right)^2 \epsilon^2_\kappa + \left(\frac{1}{\kappa y^+}\right)^2 \epsilon^2_{y^+} \\ &+ \left(\frac{1}{\kappa d^+}\right)^2 \epsilon^2_{d^+} + \epsilon^2_B + \epsilon^2_{U^+} + \epsilon^2_{\Delta U^+ fit}\end{aligned} \tag{14}$$

Equation 14 factors in the most significant error contributions, including the uncertainty in the logarithmic slope (ϵ_κ), the wall-normal location (ϵ_{y^+}), the zero-plane displacement (ϵ_{d^+}), the log-law intercept (ϵ_B), the streamwise mean velocity (ϵ_{U^+}).

Despite an ongoing debate about the universality of the Von-Kármán constants - universality between smooth and rough-wall flows, in the current study, they are assumed to be "universal". Admitting an error of 1% ($\epsilon_\kappa = 0.39 \pm 0.004$) as reported by Marusic et al (2013), the uncertainty in the log-law intercept becomes $\epsilon_B = 4.5 \pm 0.13$ meaning $\epsilon_B(\%) = 3\%$. The uncertainty in the wall-normal distance (ϵ_{y^+}) depends on the uncertainty in the friction velocity, air viscosity (itself dependent on room pressure and temperature), and PIV grid resolution. The uncertainty of the zero-plane displacement (ϵ_{d^+}) depends on the mean velocity gradient, the friction velocity, air viscosity, and the logarithmic slope. Besides the friction velocity, the uncertainty in the mean streamwise velocity (ϵ_{U^+}) also depends on both systematic and precision errors due to the limitation of the PIV reconstruction algorithm and the finite number of snapshots, respectively. Finally, the roughness function is prone to the fitting procedure, with $\epsilon_{\Delta U^+ fit}$ essentially being influenced by the extent of the log region and the number of fitted data points.

Once the uncertainty in the roughness function is determined, the error in the equivalent sand-grain roughness height can be evaluated, using either equation 7 for $\epsilon_{k_s^+}$ or equation 8 to directly assess ϵ_{k_s}. A similar linear uncertainty propagation procedure is carried out on equation 7, which yields the following expression:

$$\begin{aligned}\epsilon^2_{k_s^+} &= \left((\Delta U^+ + C)k_s^+\right)^2 \epsilon^2_\kappa \\ &+ \left(\kappa k_s^+\right)^2 \left(\epsilon^2_{\Delta U^+} + \epsilon^2_C\right)\end{aligned} \tag{15}$$

Equation 15 shows the sensitivity coefficients are expected to produce more significant errors given

the expression of k_s is based on an exponential function. This expression requires the knowledge of the overall uncertainty in the roughness function $\epsilon_{\Delta U^+}$, ϵ_κ but also ϵ_C which stems from the difference between the smooth- rough-wall log-law intercepts.

Finally, to complete the uncertainty analysis, the error in the wake strength parameter is evaluated using equation 12 which yields the following expression:

$$\epsilon^2_{\Pi^R} = \left(\frac{U^+_\infty + \Delta U^+ - B}{2}\right)^2 \epsilon^2_\kappa + \left(\frac{1}{2\delta^+}\right)^2 \epsilon^2_{\delta^+} + \left(\frac{\kappa}{2}\right)^2 \epsilon^2_{U^+_\infty} + \left(\frac{\kappa}{2}\right)^2 \epsilon^2_{\Delta U^+} + \left(\frac{\kappa}{2}\right)^2 \epsilon^2_B \quad (16)$$

In this instance, it is important to note that besides the uncertainties ϵ_κ, ϵ_B and $\epsilon_{\Delta U^+}$, equation 16 shows that ϵ_{Π^R} also depends on the uncertainty in δ^+ but more importantly the error in U^+_∞ (i.e. C_f). Hence, Π^R is inherently expected to produce larger uncertainties.

The results of the different quantities mentioned above are tabulated in 7, for both surface configurations and at all speeds examined in the wind tunnel. The results show that the roughness function is accurately measured to within ±3.5% and with the error systematically dropping down to nearly ±1.5% at the highest speeds. The overall error in the roughness Reynolds number (normalised equivalent sand-grain roughness height) is shown to be an order magnitude larger than the roughness function, with $\epsilon_{k^+_s}$ being around ±15% at low speeds, and marginally decreases to around ±10% at the highest Reynolds numbers.

Ultimately, the largest error is observed with the wake strength parameter, which exhibits errors larger than ±20% at low speeds but reduces near or below ±15%. However, it is important to recall these uncertainty estimates do not conflict with our conclusions, and they also do not necessarily imply the wake strength parameters discussed in earlier sections are erroneous. In fact, in addition to using equation 16, we have also determined the uncertainty $\epsilon_{\Pi^R,fit}$ by fitting Cole's wake function and the results clearly indicate smaller errors. The error $\epsilon_{\Pi^R,fit}$ is shown to be within ±6% or less for Config 1 and ±3% Config 2, respectively. This observation provides an additional note of caution as evidenced by how small errors from drag can propagate and can substantially impact other aerodynamic roughness parameters. Therefore, these need to be carefully considered, given the drag penalty predictions at high Reynolds numbers are shown to be influenced by the equivalent sand-grain roughness height but also the wake strength parameter.

Author contributions. TM: Formal analysis and writing of the original draft. TM, MF, RR, and BN: methodology, investigation, and data collection. JM, NH, and BG: conceptualisation, review, and editing of the manuscript. BG: funding acquisition and supervision.

Funding. The authors gratefully acknowledge the financial support from the Engineering and Physical Sciences Research Council through their grants (Ref No: EP/P009638/1 and Ref No: EP/P021476/1).

Availability of data and material. The results presented in this study will be made openly accessible on the roughness database http://roughnessdatabase.org/ and the University of Southampton repository, upon publication.

Declarations

Financial interests. The authors declare that they have no financial interests.

Non-financial interests interests. BG: is an associate editor for Experiments in Fluids. NH and BG are guest editors for this Topical Collection.

Code availability. Not applicable.

Ethical approval. Not applicable.

Consent to participate. Not application.

Consent for publication. All authors have given their explicit consent to submit.

References

Acharya M, Bornstein J, Escudier MP (1986) Turbulent boundary layers on rough surfaces. Exp Fluids 4(1):33–47. URL https://doi.org/10.1007/BF00316784

Amir M, Castro IP (2011) Turbulence in rough-wall boundary layers: universality issues. Exp Fluids 51(2):313–326

Table 7 Overall uncertainty estimates of the aerodynamic parameters as measured directly using the floating-element drag balance and the velocity profiles from PIV/sPIV, for both surface configurations. The uncertainty $\epsilon_{\Pi^R,fit}$ is determined by using equation 1, and fitting Cole's wake function to the velocity profiles, whereas ϵ_{Π^R} is simply the overall uncertainty evaluated from equation 16.

Case	Data	U_∞ (ms^{-1})	$\epsilon_{\Delta U^+}$ (%)	$\epsilon_{k_s^+}$ (%)	$\epsilon_{\Pi^R,fit}$ (%)	ϵ_{Π^R} (%)
Config 1	PIV_v	07.76	2.50	12.88	5.08	22.58
	PIV_v	10.29	2.14	11.89	2.56	22.16
	PIV_v	12.75	2.00	11.79	5.77	20.81
	PIV_v	18.05	3.14	18.12	6.84	23.27
	PIV_v	23.07	1.52	10.75	5.42	14.01
	PIV_p	23.82	1.37	10.15	5.73	13.64
	$sPIV_p$	18.24	2.17	13.25	6.57	18.41
Config 2	$sPIV_p$	07.60	3.76	16.69	1.88	27.51
	$sPIV_p$	10.35	2.84	13.97	1.46	23.24
	$sPIV_p$	13.70	2.71	14.07	2.40	24.87
	$sPIV_p$	18.09	2.11	12.13	2.10	19.18
	$sPIV_p$	23.07	1.81	11.29	3.60	16.02
	PIV_p	18.07	1.71	10.44	3.11	18.01
	PIV_v	18.15	2.32	13.13	2.16	19.02

Andreopoulos J, Bradshaw P (1981) Measurements of turbulence structure in the boundary layer on a rough surface. Boundary Layer Meteorol 20(2):201–213. URL https://doi.org/10.1007/BF00119902

Baars W, Squire D, Talluru K, et al (2016) Wall-drag measurements of smooth-and rough-wall turbulent boundary layers using a floating element. Exp Fluids 57(5):90

Castro IP (2007) Rough-wall boundary layers: mean flow universality. J Fluid Mech 585:469––485

Castro IP, Segalini A, Alfredsson PH (2013) Outer-layer turbulence intensities in smooth- and rough-wall boundary layers. J Fluid Mech 727:119–131

Chan L, MacDonald M, Chung D, et al (2018) Secondary motion in turbulent pipe flow with three-dimensional roughness. J Fluid Mech 854:5–33. https://doi.org/10.1017/jfm.2018.570

Cheng H, Castro PI (2002) Near wall flow over urban-like roughness. Boundary-layer Meteorol 104(2):229–259

Chung D, Monty JP, Hutchins N (2018) Similarity and structure of wall turbulence with lateral wall shear stress variations. J Fluid Mech 847:591–613. https://doi.org/10.1017/jfm.2018.336

Chung D, Hutchins N, Schultz MP, et al (2021) Predicting the drag of rough surfaces. Annu Rev Fluid Mech 53:439–471

Clauser FH (1956) The turbulent boundary layer. Adv Appl Mech 4:1–51

Colebrook CF, White CM (1937) Experiments with fluid friction in roughened pipes. Philos Trans Royal Soc A Math Phys Eng Sci 16:367–381

Coles D (1956) The law of the wake in the turbulent boundary layer. J Fluid Mech 1:191—226

Ferreira M, Ganapathisubramani B (2021) Scale interactions in velocity and pressure within a turbulent boundary layer developing over a staggered-cube array. J Fluid Mech 910:A48

Ferreira MA, Rodriguez-Lopez E, Ganapathisubramani B (2018) An alternative floating element

design for skin-friction measurement of turbulent wall flows. Exp Fluids 59:155

Flack KA, Schultz MP, Shapiro TA (2005) Experimental support for Townsend's Reynolds number similarity hypothesis on rough walls. Phys Fluids 17(3):35,102. https://doi.org/10.1063/1.1843135

Flack KA, Schultz MP, Connelly JS (2007) Examination of a critical roughness height for outer layer similarity. Phys Fluids 19(9):95,104

Granville PS (1987) Three indirect methods for the drag characterization of arbitrarily rough surfaces on flat plates. J Ship Res 31:70 – 77

Guo J, Julien PY, Meroney RN (2005) Modified log-wake law for zero-pressure-gradient turbulent boundary layers. J Hydraul Res 43(4):421–430. https://doi.org/10.1080/00221680509500138, URL https://doi.org/10.1080/00221680509500138, https://arxiv.org/abs/https://doi.org/10.1080/00221680509500138

Hama FR (1954) Boundary-layer characteristics for smooth and rough surfaces. Trans Soc Nav Archit Mar Engrs 1:333–358

Hinze J (1975) Turbulence /2nd edition/. McGraw Hill, New York

Hutchins N, Ganapathisubramani B, Schultz M, et al (2023) Defining an equivalent homogeneous roughness length for turbulent boundary layers developing over patchy or heterogeneous surfaces. Ocean Eng 271:113,454

Jackson PS (1981) On the displacement height in the logarithmic velocity profile. J Fluid Mech 111:15–25

Jimenez J (2004) Turbulent flows over rough walls. Annu Rev Fluid Mech 36:173–196.

Jones MB, Marusic I, Perry AE (2001) Evolution and structure of sink-flow turbulent boundary layers. J Fluid Mech 428:1–27. https://doi.org/10.1017/S0022112000002597

Krogstad P, Antonia RA, Browne LWB (1992) Comparison between rough- and smooth-wall turbulent boundary layers. J Fluid Mech 245:599–617

Krogstad PA, Antonia RA (1994) Structure of turbulent boundary layers on smooth and rough walls. J Fluid Mech 277:1–21. https://doi.org/10.1017/S0022112094002661

Krogstad PÅ, Efros V (2010) Rough wall skin friction measurements using a high resolution surface balance. Intl J Heat Fluid Flow 31(3):429–433

Krug D, Philip J, Marusic I (2017) Revisiting the law of the wake in wall turbulence. J Fluid Mech 811:421–435. https://doi.org/10.1017/jfm.2016.788

Lee J, Monty J, Hutchins N, et al (2016) Validating under-resolved turbulence intensities for piv experiments in canonical wall-bounded turbulence. Exp Fluids 57(8):1–11

Marusic I, Monty JP, Hultmark M, et al (2013) On the logarithmic region in wall turbulence. J Fluid Mech 716:R3

Medjnoun T, Vanderwel C, Ganapathisubramani B (2018) Characteristics of turbulent boundary layers over smooth surfaces with spanwise heterogeneities. J Fluid Mech 838:516–543. https://doi.org/10.1017/jfm.2017.849

Medjnoun T, Vanderwel C, Ganapathisubramani B (2020) Effects of heterogeneous surface geometry on secondary flows in turbulent boundary layers. J Fluid Mech 886:A31. https://doi.org/10.1017/jfm.2019.1014

Medjnoun T, Rodriguez-Lopez E, Ferreira M, et al (2021) Turbulent boundary-layer flow over regular multiscale roughness. J Fluid Mech 917:A1

Moffat RJ (1988) Describing the uncertainties in experimental results. Exp Therm Fluids Sci 1(1):3–17

Monty JP, Dogan E, Hanson R, et al (2016) An assessment of the ship drag penalty arising from light calcareous tubeworm fouling. Biofouling

32:451–464

Nagib HM, Chauhan KA (2008) Variations of von kármán coefficient in canonical flows. Phys Fluids 20(10):101,518. https://doi.org/10.1063/1.3006423, URL https://doi.org/10.1063/1.3006423, https://arxiv.org/abs/https://doi.org/10.1063/1.3006423

Nagib HM, Chauhan KA, Monkewitz PA (2007) Approach to an asymptotic state for zero pressure gradient turbulent boundary layers. Phil Trans R Soc Lond A 365(1852):755–770

Napoli E, Armenio V, De Marchis M (2008) The effect of the slope of irregularly distributed roughness elements on turbulent wall-bounded flows. J Fluid Mech 613:385–394. https://doi.org/10.1017/S0022112008003571

Nikuradse J (1933) Stromungsgesetze in rauhen rohren. VDI-Forsch 361:1

Österlund JM, Johansson AV, Nagib HM, et al (2000) A note on the overlap region in turbulent boundary layers. Phys Fluids 12(1):1–4

Perry AE, Abell CJ (1977) Asymptotic similarity of turbulence structures in smooth- and rough-walled pipes. J Fluid Mech 79(4):785–799. https://doi.org/10.1017/S0022112077000457

Perry AE, Li JD (1990) Experimental support for the attached-eddy hypothesis in zero-pressure-gradient turbulent boundary layers. J Fluid Mech 218:405–438. https://doi.org/10.1017/S0022112090001057

Raupach M (1992) Drag and drag partition on rough surfaces. Boundary-Layer Met 60(4):375–395

Schultz M, Myers A (2003) Comparison of three roughness function determination methods. Exp Fluids 35(4):372–379

Schultz MP (2007) Effects of coating roughness and biofouling on ship resistance and powering. Biofouling 23(5):331–341

Schultz MP, Flack KA (2005) Outer layer similarity in fully rough turbulent boundary layers. Exp Fluids 38(3):328–340. https://doi.org/10.1007/s00348-004-0903-2

Schultz MP, Flack KA (2009) Turbulent boundary layers on a systematically varied rough wall. Phys Fluids 1:015,104

Sillero JA, Jiménez J, Moser RD (2013) One-point statistics for turbulent wall-bounded flows at reynolds numbers up to $\delta^+ \approx 2000$. Phys Fluids 25(10):105,102. https://doi.org/10.1063/1.4823831, URL https://doi.org/10.1063/1.4823831, https://arxiv.org/abs/https://doi.org/10.1063/1.4823831

Squire DT, Morrill-Winter C, Hutchins N, et al (2016) Comparison of turbulent boundary layers over smooth and rough surfaces up to high reynolds numbers. J Fluid Mech 795:210–240

Townsend AA (1976) The structure of turbulent shear flow. Cambridge University Press

Volino RJ, Schultz MP (2018) Determination of wall shear stress from mean velocity and reynolds shear stress profiles. Phys Rev Fluids 3(3):034,606

Volino RJ, Schultz MP, Flack KA (2009) Turbulence structure in a boundary layer with two-dimensional roughness. J Fluid Mech 635:75–101

Womack KM, Meneveau C, Schultz MP (2019) Comprehensive shear stress analysis of turbulent boundary layer profiles. J Fluid Mech 879:360–389

Womack KM, Volino RJ, Meneveau C, et al (2022) Turbulent boundary layer flow over regularly and irregularly arranged truncated cone surfaces. J Fluid Mech 933:A38

Wu Y, Christensen KT (2007) Outer-layer similarity in the presence of a practical rough-wall topography. Phys Fluids 19(8)